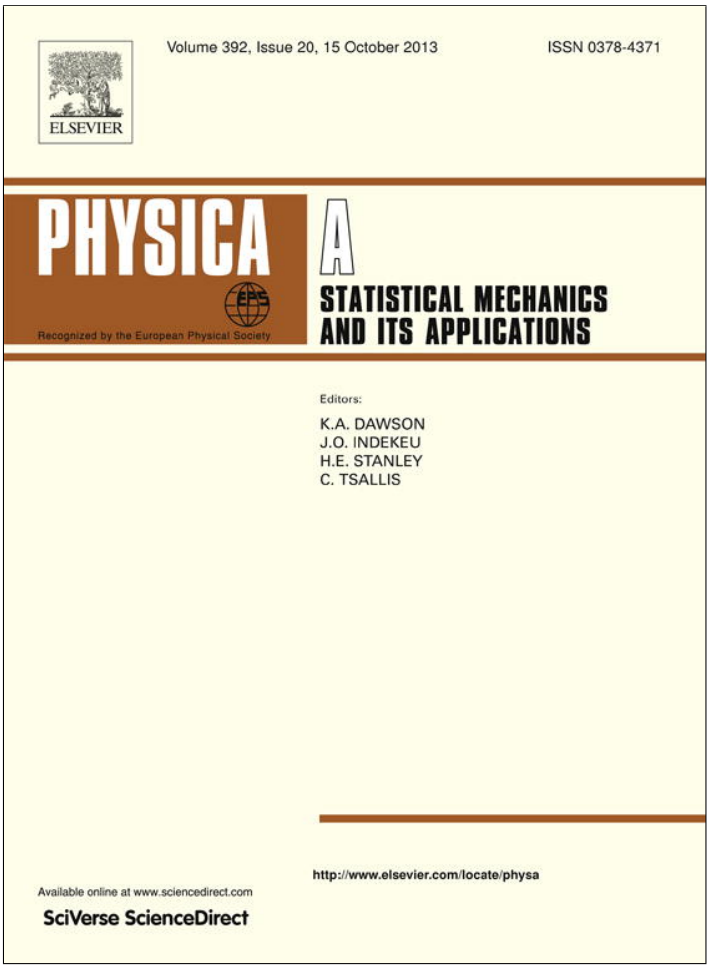

Physica A 392 (2013) 4946–4955

Contents lists available at SciVerse ScienceDirect

Physica A

journal homepage: www.elsevier.com/locate/physa

Lag-driven motion in front propagation

Daniel R. Amor *, Joaquim Fort

Complex Systems Laboratory and Physics Department, University of Girona, 17071 Girona, Catalonia, Spain

HIGHLIGHTS

- An approximate front speed holds for systems presenting time-delayed dispersal.
- The approximate front speed explains the observed spread of several focal infections.
- Approximate spread rates for the Neolithic transition agree with observed data.
- Observed spread rates of tree colonizations are predicted by our approximate speed.
- The approximate speed is derived from the equations for the three systems above.

ARTICLE INFO

Article history:
Received 5 March 2013
Available online 2 July 2013

Keywords:
Front propagation
Reaction–diffusion equations
Molecular dynamics simulations
Biological invasions

ABSTRACT

Front propagation is a ubiquitous phenomenon. It arises in physical, biological and cross-disciplinary systems as diverse as flame propagation, superconductors, virus infections, cancer spread or transitions in human prehistory. Here we derive a single, approximate front speed from three rather different time-delayed reaction–diffusion models, suggesting a general law. According to our approximate speed, fronts are crucially driven by the lag times (periods during which individuals or particles do not move). Rather surprisingly, the approximate speed is able to explain the observed spread rates of completely different biophysical systems such as virus infections, the Neolithic transition in Europe, and postglacial tree recolonizations.

1. Introduction

Fronts are widely used in physical models of flame propagation [1], superconductors [2], virus infections [3], cancer spread [4], transitions in human prehistory [5], etc. In many systems, individuals or particles are at rest during some time intervals, and for this reason the corresponding fronts become time-delayed [5]. For single-species systems, the dynamics is governed by the hyperbolic reaction–diffusion (HRD) equation [6]:

$$\frac{\delta p}{\delta t}+\frac{T}{2}\frac{\delta^2 p}{\delta t^2}=D\left(\frac{\delta^2 p}{\delta x^2}+\frac{\delta^2 p}{\delta y^2}\right)+\left.\frac{\delta p}{\delta t}\right|_g+\left.\frac{T}{2}\frac{\delta^2 p}{\delta t^2}\right|_g, \tag{1}$$

where $p=p(x,y,t)$ is the population (or particle) number density at point (x,y) and time t, D is the diffusion coefficient, and the subindex $\cdots|_g$ indicates that the corresponding time derivatives take into account growth (i.e., net reproductive) but not diffusive processes [6]. In Eq. (1), terms proportional to T are second-order Taylor expansion terms [6] and account for the effects of the delay (or lag) time T which is elapsed between two successive motions of particles or individuals. If no delay time is considered (i.e., if $T=0$), Fisher's classical reaction–diffusion equation [7] is recovered.

A set of coupled equations is required when extending the scope to multiple-species systems. For example, focal infections provide a convenient experimental platform to study the replication (reaction) and spread (diffusion) of viruses

* Corresponding author.
E-mail addresses: daniel.r.amor@gmail.com, daniel.rodriguez@udg.edu (D.R. Amor).

0378-4371/$ – see front matter
http://dx.doi.org/10.1016/j.physa.2013.06.058

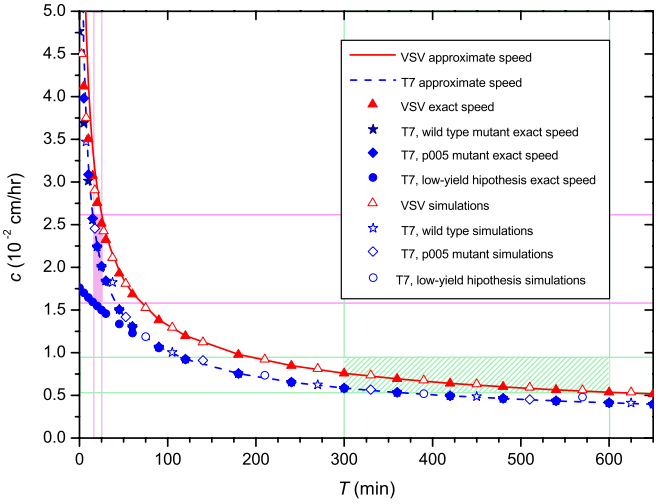

Fig. 1. Focal infections. Front speed versus lag time. The curves stand for the approximate solution $c = \sqrt{2D/T}$. The solid curve corresponds to VSV ($D = 1.44 \cdot 10^{-4}$ cm^2/h) and the dashed curve to the two T7 mutants ($D = 8.55 \cdot 10^{-5}$ cm^2/h). The full (empty) symbols correspond to the results of the exact theory (simulations). The triangles represent the results for VSV ($Y = 4983$ [11]). The stars stand for the wild T7 strain ($Y = 34.5$ [3]), and the rhombus for the p005 T7 mutant ($Y = 63.6$). The circles represent a hypothetical low-yield case $Y = 5$. The hatched (shaded) area corresponds to the observed ranges of T and c for VSV (T7) viruses. Details on the parameter values and the simulations appear in Appendix A.

in a cell monolayer [3,8,9]. The interactions between viruses (V), non-infected cells (C) and infected cells (I) give rise to the following evolution equations [3,10,11]:

$$\frac{\partial [C]}{\partial t} = -k_1 [C][V], \tag{2}$$

$$\frac{\partial [I]}{\partial t} = k_1 [V][C] - k_2 [I] \left(1 - \frac{[I]}{I_{\mathrm{MAX}}}\right), \tag{3}$$

where k_1 stands for the rate constant of adsorption of viruses V to non-infected cells C and k_2 is the death (or lysis) rate of infected cells I (each infected cell releases a new generation of Y viruses after a delay time T). If we replace p by the virus number density $[V](r, t)$ (where r is the radial coordinate centered at the inoculation point of the infection) in the above HRD equation (1), we obtain the evolution equation for the virus population. In agreement with Eqs. (2)–(3), the virus population growth reads

$$\left.\frac{\delta [V]}{\delta t}\right|_g = -k_1 [V][C] + k_2 Y [I] \left(1 - \frac{[I]}{I_{\mathrm{MAX}}}\right). \tag{4}$$

Hence, in order to determine the dynamics of focal infections, the set of differential equations (1)–(4) must be solved. Whereas the exact speed of front solutions to Eqs. (1)–(4) is very complicated (see Appendix A), recently we derived an approximate solution for the spread of virus infections which reads [11][1]

$$c = \sqrt{2D/T}. \tag{5}$$

Note that dimensional analysis could also suggest that c is proportional to $\sqrt{D/T}$, but other dependences are possible on this ground, e.g. $\sqrt{k_2 D}$ for Eqs. (1)–(4), $\sqrt{aD}$ (Fisher's speed [7]), $\sqrt{a^2 D/T}$ for Eq. (1), etc. Moreover, dimensional analysis cannot predict the factor $\sqrt{2}$, which was derived by marginal stability analysis in Ref. [11].

We would like to emphasize the following physical interpretation of Eq. (5). First, the parameter T is defined as the mean time a virus needs to reproduce inside an infected cell. If this lag T is substantially longer than the rest of the interval times involved in a virus life cycle (i.e., the death time of cells k_2^{-1}, the mean travel time in the extracellular medium, and the time viruses need to cross the cell membrane $k_1^{-1} C_0^{-1}$), then T becomes the only relevant time scale in our model. On the other hand, the parameter D is related to how easily the virus diffuses in the extracellular medium. It is thus reasonable that the parameters T and D determine the front speed under these assumptions. But is this framework valid in real situations? Before closing this introduction, we address this question by applying Eq. (5) to several virus infections.

Fig. 1 compares the results from the approximate speed (5), the exact theory, and simulations for the front speed of focal infections for Vesicular Stomatitis Virus (VSV) [11]. Moreover, for the first time Eq. (5) is applied to the T7 virus [3]: in Fig. 1

[1] In Ref. [11] we presented an approximate infection front speed in dimensionless variables which is equivalent to Eq. (5) in the present paper.

we present results for two T7 strains, namely the wild type and the p005 mutant [9]. Both for T7 and VSV, perfect agreement between the exact result (which is rather complicated, see Appendix A) and the approximate speed (5) is observed. Hence Eq. (5) provides convenient results to predict virus infection speeds. Moreover, both exact and approximate results in Fig. 1 show consistency with the corresponding experimental data (shaded rectangles).

The main aims of the present paper are (i) to derive mathematically the same approximate Eq. (5) for two other systems, which are driven by equations completely different to the virus reaction–diffusion equations (1)–(4), and (ii) to show that a fair agreement with observations can be attained also for those two additional systems. Accordingly, in Section 2 we consider a single-population model (and apply it to the Neolithic transition front in Europe) and in Section 3 we analyze a structured population model (and apply it to forest recolonization fronts).

2. Approximate front speed for non-structured populations

Two major processes drive the spatial population dynamics of biophysical systems: population growth (reproduction minus deaths) on one hand, and migration (dispersal) on the other. In many cases, these two processes can be considered independent of each other. Typically, such an assumption is implicit in the study of non-structured populations [5,6]. Within this framework, in this section we derive an approximate front speed from reaction–diffusion equations applied to non-structured population systems involving a single species. For the sake of clarity, we first review briefly the derivation of the HRD speed [5,6].

The variation of the population number density due to population growth can be generally expressed as a Taylor series,

$$[p(x,y,t+T)-p(x,y,t)]_g = T\left.\frac{\delta p}{\delta t}\right|_g + \frac{T^2}{2}\left.\frac{\delta^2 p}{\delta t^2}\right|_g + \cdots \tag{6}$$

where the subindex $\cdots|_g$ indicates that the corresponding time derivatives take into account growth (i.e., net reproductive) but not migration processes [6]. In most biological applications the lag T corresponds to one generation [5] (see, e.g., the lag time in focal infections above).

In order to account for migration (dispersal), it is useful to define the dispersal kernel $\phi(\Delta_x, \Delta_y)$ as the probability per unit area that an individual initially placed at $(x+\Delta_x, y+\Delta_y)$ has reached the position (x,y) after a time T. This leads to the following change for the population density due to the migration process [5,6],

$$[p(x,y,t+T)-p(x,y,t)]_m = \int_{-\infty}^{+\infty}\int_{-\infty}^{+\infty} p(x+\Delta_x, y+\Delta_y, t)\phi(\Delta_x,\Delta_y)\mathrm{d}\Delta_x\,\mathrm{d}\Delta_y - p(x,y,t). \tag{7}$$

Thus, the evolution of a system involving both processes (i.e., population growth and migration) is driven by the sum of both contributions,

$$p(x,y,t+T) = \int_{-\infty}^{+\infty}\int_{-\infty}^{+\infty} p(x+\Delta_x, y+\Delta_y, t)\,\phi(\Delta_x,\Delta_y)\mathrm{d}\Delta_x\,\mathrm{d}\Delta_y + T\left.\frac{\delta p}{\delta t}\right|_g + \frac{T^2}{2}\left.\frac{\delta^2 p}{\delta t^2}\right|_g + \cdots \tag{8}$$

If isotropic migration is assumed (i.e., if $\phi(\Delta_x,\Delta_y)=\phi(\Delta)$, with $\Delta=\sqrt{\Delta_x^2+\Delta_y^2}$), then Taylor-expanding the above Eq. (8) up to second order in time and space yields the HRD equation (1). The diffusivity of the population in the HRD equation is defined as $D=\frac{\langle\Delta^2\rangle}{4T}$ [5]. In order to solve the HRD equation, it is convenient to define $F(p)$ as the population growth function $F(p)=\left.\frac{\delta p}{\delta t}\right|_g$. Assuming (i) low population densities at the leading edge of the front, (ii) that the front is locally planar for $t\to\infty$ and $r\to\infty$, and (iii) constant-shape solutions with the form $p=\bar{p}\exp[\lambda(x-ct)]$, then the exact solution of Eq. (1) yields the HRD front speed, namely [6]

$$c=\frac{2\sqrt{DF'(0)\left[1+\frac{T}{2}F'(0)\right]}}{1+TF'(0)}, \tag{9}$$

where the growth rate at the front's edge has been approximated as $F'(0)=\left.\frac{dF}{dp}\right|_{p=0}$.

Let us now consider the limiting case of a high reproduction rate, $F'(0)\to\infty$, into the above Eq. (9). This leads to the very simple expression

$$c=\sqrt{2D/T}. \tag{10}$$

Remarkably, this simple approach has led us to the very same approximate front speed as for the case of focal infections above (see Eq. (5)). It is worth noting that the single-species systems analyzed in this section are very different (both mathematically and physically) from the focal infections considered in the introduction (in which the equations of the system must account for the interactions between three species, so a set of coupled equations is involved instead of a single equation).

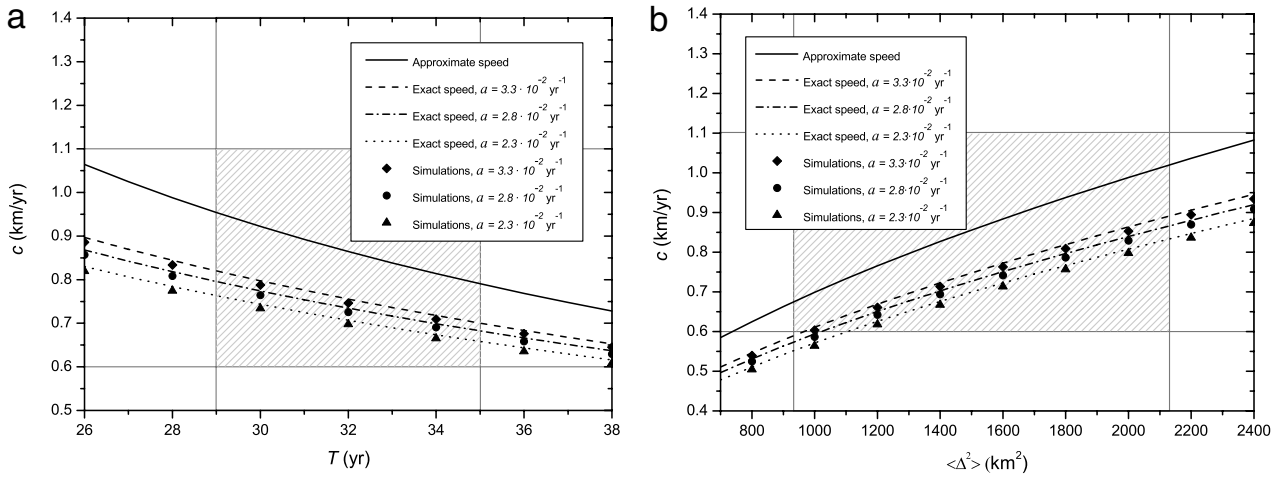

Fig. 2. The Neolithic transition. (a) Invasion front speed versus T (using $\langle\Delta^2\rangle = 1531\,\mathrm{m}^2$ [14]). The solid curve corresponds to the approximate $c = \sqrt{2D/T}$. The dashed–dotted curve represents the exact theoretical speed (9) for the mean observed value $a = 2.8 \cdot 10^{-2}\ \mathrm{yr}^{-1}$ [14]. The dashed and dotted curves stand for the maximum ($a = 3.3 \cdot 10^{-2}\ \mathrm{yr}^{-1}$) and minimum ($a = 2.3 \cdot 10^{-2}\ \mathrm{yr}^{-1}$) values of the observed range, respectively. The symbols correspond to numerical simulations as indicated in the legend (see Appendix B for details on the simulations). The hatched area indicates the observed ranges of T [15] and c [12]. (b) Invasion front speed versus the mean-squared migration distance. The curves and the symbols stand for the same cases presented in (a), but for $T = 32$ yr. The hatched rectangle represents the observed ranges of $\langle\Delta^2\rangle$ and c [12,14].

Let us now apply the HRD equation [6] to the invasion front of the Neolithic transition, in order to check the results of the approximate speed $c = \sqrt{2D/T}$. Previous HRD models for this single-species system [5,6] have shown good agreement with the observed dates from hundreds of European Neolithic sites [12]. Applying the HRD exact speed (9) involves the computation of the Neolithic population growth function. For this purpose, we consider the logistic growth function, which agrees very well with many human populations [5,13], namely

$$F(p) = \left.\frac{\delta p}{\delta t}\right|_g = ap\left(1 - \frac{p}{p_{\max}}\right), \tag{11}$$

where a is called the initial growth rate and $p_{\max}$ is the saturation density. Note that considering logistic growth leads to $F'(0) = a$.

Fig. 2a plots the invasion speed of the Neolithic transition as a function of T. In this case, T represents the generational lag during which children stay with their parents until they reach adulthood and can migrate [15]. Fig. 2b plots the Neolithic front speed as a function of the mobility $\langle\Delta^2\rangle$ [14]. In both Fig. 2a and b we observe differences (about 15%) between the approximate speed (5) and the exact solution (9) if the mean observed growth rate $a = 0.028\ \mathrm{yr}^{-1}$ [14,16–18] is considered. Interestingly, both the approximate and the exact solutions are consistent with the observed invasion speed of the Neolithic front, as estimated from archeological data (hatched area in Fig. 2a–b) [12,15].

3. Approximate front speed for structured populations

In some biophysical systems, the age structure of the population plays a major role on the evolution of the system [19–21]. In some cases (e.g., for tree species), the fertile ages of several generations widely overlap. Thus it is necessary to introduce $p_i(x, y, t)$ as the number density of the subpopulation which is i years old ($i = 1, 2, \ldots, N$). The system dynamics is then controlled by the vector equation [19]

$$\vec{p}\,(\Delta x, \Delta y, t+1) = \int_{-\infty}^{+\infty}\int_{-\infty}^{+\infty} \vec{\vec{\Phi}} \circ \vec{\vec{A}} \cdot \vec{p}\,(x+\Delta_x, y+\Delta_y, t)\mathrm{d}\Delta_x\mathrm{d}\Delta_y, \tag{12}$$

where $\left(\vec{\vec{\Phi}} \circ \vec{\vec{A}}\right)_{ij} = \Phi_{ij}A_{ij}$. The elements A_{ij} of the demographic matrix $\vec{\vec{A}}$ describe the rate at which an individual in state j gives rise to individuals in state i per unit time. Similarly, the elements Φ_{ij} of the dispersal matrix $\vec{\vec{\Phi}}$ indicate the probability that an individual moves from $(x+\Delta_x, y+\Delta_y)$ to (x, y) when its stage changes from j to i. For example, any adult tree which is j years old will be $j+1$ one year after (i.e., after t has increased to $t+1$). Thus $A_{ij} = 1$ if $i = j+1$. However, trees cannot move, so $\Phi_{ij} = \delta_{2D}(\Delta)$ if $i = j+1$ (where $\delta_{2D}(\Delta)$ is the 2-dimensional Dirac delta centered at $\Delta = 0$). Indeed, a single stage could be used to represent several years in the life of an individual (as in some structured population models [20,21]), but this would not significantly change the discussion below. In Eq. (12) growth and dispersal are not necessarily independent processes, in contrast to the case in the previous section. For example, note that for tree populations only seeds are dispersed, hence dispersal immediately follows reproduction [19,22] (see also Appendix C).

For clarity, let us briefly recall that the exact solution for the front speed from the evolution equation (12) is derived as follows by looking for constant-shape solutions for each subpopulation, $p_i(x, y, t) = w_i \exp[-\lambda(x - ct)]$. Using this into Eq. (12) yields

$$\exp(\lambda c)\overrightarrow{w} = \left(\int_{-\infty}^{+\infty}\int_{0}^{+\infty} \overrightarrow{\overrightarrow{\Phi}} \circ \overrightarrow{\overrightarrow{A}} \exp\left[-\lambda r\cos\theta\right] \, dr d\theta\right)\overrightarrow{w}\,, \tag{13}$$

and the exact theoretical front speed is given by [19]

$$c = \min_{\lambda} \frac{\ln\left[\rho_1(\lambda)\right]}{\lambda}, \tag{14}$$

where ρ_1 is the largest real of the eigenvalues of the matrix $\int_0^{+\infty} \overrightarrow{\overrightarrow{\Phi}} \circ \overrightarrow{\overrightarrow{A}} \exp\left[-\lambda r\cos\theta\right] \, dr d\theta$.

Given the substantial complexity of Eq. (13), an explicit expression for the exact front speed cannot be derived. For instance, the high lifespan of trees can lead both $\overrightarrow{\overrightarrow{A}}$ and $\overrightarrow{\overrightarrow{\Phi}}$ to be of order above 100 when applying the model to tree recolonizations [19]. For this reason, we need to make some simplifying assumptions in order to derive an approximate expression for the front speed (later we will assess the validity of our assumptions by comparing to the exact speed (14)). First, we assume that the following non-structured equation [22] provides an approximately valid description of the evolution of the structured population at the leading edge of the front:

$$p(x, y, t + T) = R_{0g}\int_{-\infty}^{+\infty}\int_{-\infty}^{+\infty} p(x + \triangle_x, y + \triangle_y, t)\ \phi(\triangle_x, \triangle_y) d\triangle_x \ d\triangle_y, \tag{15}$$

where R_{0g} is the generational initial growth rate (i.e., the average reproductive rate per individual and generation). Note that a major effect of considering the structure of the population (i.e., Eq. (12) instead of Eq. (15)) is that the reproduction of elder individuals is taken into account. However, such contribution to the population growth has been shown to play a minor role on the front speed when reproduction rates are above a certain threshold [19], because then the reproduction at the leading edge of the front is mainly produced by young individuals. Thus, if we assume a fast growth rate it is reasonable to expect that Eq. (12) can be approximated by the non-structured Eq. (15). Next, we Taylor-expand Eq. (15) up to second order in time and space and obtain

$$\frac{\delta p}{\delta t} + \frac{T}{2}\frac{\delta^2 p}{\delta t^2} = \frac{(R_{0g} - 1)}{T}p(x, y, t) + D\left(\frac{\delta^2 p}{\delta x^2} + \frac{\delta^2 p}{\delta y^2}\right), \tag{16}$$

where $D = R_{0g}\langle\Delta^2\rangle/4T$. As usual, we look for solutions with the form $p = p_0 \exp[-\lambda(x - ct)]$ with $\lambda > 0$. Using this into Eq. (16) yields

$$\lambda = \frac{Tc \pm \sqrt{(Tc)^2 - 4(R_{0g} - 1)\left(DT - \frac{T^2c^2}{2}\right)}}{2\left(DT - \frac{T^2c^2}{2}\right)}, \tag{17}$$

and, assuming as usual that the minimum speed is the one of the front [23], we obtain

$$c = \left(\frac{2D}{T\left(1 + \frac{1}{2(R_{0g}-1)}\right)}\right)^{1/2}. \tag{18}$$

Since we are considering high values of the reproduction rate, we assume that the condition $1 \gg \left(2(R_{0g} - 1)\right)^{-1}$ is satisfied in Eq. (18). Interestingly, this finally simplifies into the same approximate front speed as that in the previous two sections, namely

$$c = \sqrt{2D/T}. \tag{19}$$

It is worth noting that in Eq. (15) dispersal (of seeds) occurs immediately after reproduction (this is a major feature of tree populations). This is why the diffusivity D in this section (see its definition below Eq. (16)) depends on the growth rate R_{0g}. For the applications to postglacial recolonizations below, we consider $R_{0g} = TR_0$ (where R_0 is the average reproduction rate per tree and year). In other words, we assume that R_{0g} corresponds to the sum of the seasonal fecundities of the T reproduction events in which a parent tree is involved before individuals of the next generation become adults.[2] Details on the empirical data for the tree species considered below, as well as the definition of the matrix elements A_{ij} and ϕ_{ij}, are presented in Appendix C.

[2] This is a smoother approach than those in some previous nonoverlapping-generations models, such as considering $R_{0g} = R_0$ [22,19], or assuming R_{0g} is equal to R_0 times a mean fertile age [24].

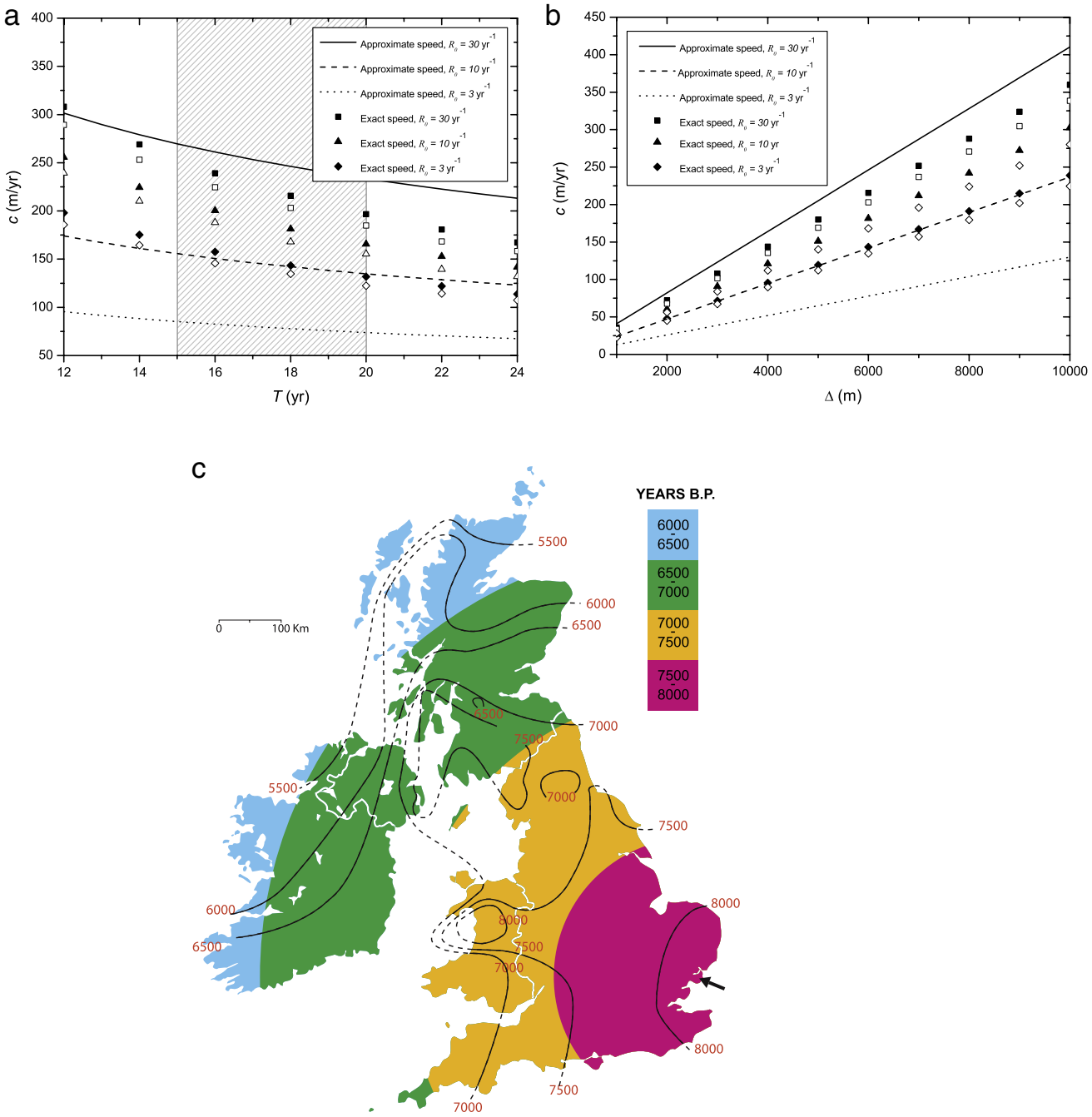

Fig. 3. Postglacial recolonizations. (a) Invasion front speed versus lag time for the yellow poplar ($\Delta = 6000$ m). The solid, dashed and dotted curves stand for the approximate $c = \sqrt{2D/T}$, for the cases $R_0 = 30$, 10 and 3 yr^{-1}, respectively. The probability $(1 - p_e)$ for long-distance dispersals (with $p_e = 0.99798$ [22]) has been taken into account when computing $\langle \Delta^2 \rangle$. The full (empty) squares, triangles and rhombus correspond to the exact theoretical solutions (numerical simulations) for $R_0 = 30$, 10 and 3 yr^{-1}, respectively. The hatched rectangle is the observed range of T [25]. Additional information on simulations and empirical data is provided in Appendix C. (b) Invasion front speed versus seed dispersal distance. The lines and symbols correspond to the same cases in (a), but for $T = 18$ yr [25]. (c) Black alder postglacial recolonization of the British Isles (color online). Colored regions depict the predicted arrival times for an invasion with the constant speed $c = 462$ m/yr, computed from Eq. (5) with $T = 6$ yr [26], $\Delta = 6500$ m [27], $p_e = 0.99798$ and $R_0 = 30$. The black isochrone curves correspond to those inferred from pollen data by H. Birks in Ref. [28]. The arrow indicates the direction of arrival of black alder trees into the British Isles [28].

Fig. 3a shows the exact speed for the overlapping-generations model (14) and three values within the observed range of R_0 for the yellow poplar (*Liriodendron tulipifera)* species, which was previously used to study postglacial recolonization fronts [19,22]. Both the exact theory and the simulations in Fig. 3a are in good agreement (the observed differences, about 7%, are due to the discretization of the space in the simulations [19]). In Fig. 3a, within the observed range of T, the differences between approximate (5) and exact (14) theory are below 15% for the case $R_0 = 30$ yr^{-1} (the lower reproduction rates $R_0 = 10$ yr^{-1} and $R_0 = 3$ yr^{-1} present higher differences). However, if $R_0 \geq 10$ yr^{-1} the approximate, exact and numerical front speeds all lay within 10^2–10^3 m/yr (which is the observed range for postglacial recolonizations [29]). On the other hand,

long-distance dispersal events (due to atmospheric turbulence) have been shown to spread seeds along distances $\Delta \sim 10^3$–10^4 m for this species [30,31].[3] The front speed dependence on the seed dispersal distance Δ is shown in Fig. 3b. Remarkably, if the reactive process is fast enough (curve for $R_0 = 30\ \mathrm{yr}^{-1}$) then the approximate solution derived above, Eq. (19), closely agrees with the exact solution to Eq. (14), which is very complicated mathematically (see the discussion above). Furthermore, for $R_0 = 30\ \mathrm{yr}^{-1}$ and $\Delta > 3000$ m we observe predicted speeds within the observed range for postglacial recolonizations (10^2–10^3 m/yr) [29]. Finally, in Fig. 3c we have applied our approximate Eq. (5) to model the Holocene invasion of the black alder *(Alnus glutinosa),* across the British Isles [28]. Obviously, the invasion predicted by Eq. (5) gives a circular-shaped front, corresponding to a constant speed. Although admittedly simple, this approximate front is in remarkable agreement with the observed colonization dates of the black alder, specially for the isochrones $\geq$ 6500 yr before present (BP). The slowdown of the observed invasion front when reaching high latitudes (<6500 yr BP) is not surprising, because such a slowdown is observed in many tree species and could be due to adaptations to the harsher northern climate [28].

4. Discussion

When studying the three systems presented above, we observe the following general trend: the higher the reproduction rate (i.e., Y in Fig. 1, a in Fig. 2, and R_0 in Fig. 3a and b), the closer our approximate speed $c = \sqrt{2D/T}$ is to the corresponding exact solution. For virus infections, both the VSV and the T7 display high enough values of Y and Eq. (5) agrees well with observations. In contrast, when introducing the hypothetical low-yield case where $Y = 5$ (circles in Fig. 1), the approximate speed does not provide accurate results for $T < 60$ min. This is not a problem at all (because such values of Y and T are far below the observations for T7 [9]).[4]

The approximate speed (5), originally derived for a very special case (namely focal infection systems), has been shown here to be valid for a wide range of systems, from non-structured single-species systems (Section 2) to rather complicated structured systems (Section 3). In all of those cases, we have also shown that observations agree reasonably well with our approximate Eq. (5). Thus, we find many substantially different systems with the same front speed (5) and, remarkably, this makes all parameter values related to the reactive processes (a, Y, k_1, k_2, R_0, etc.) irrelevant. Obviously, this enormously simplifies the task of comparing theory and experiment.

In this paper we have analyzed a wide variety of propagating fronts in biophysical systems, where the lag time T plays an important role in the system dynamics. We have shown that the approximate speed $c = \sqrt{2D/T}$ provides convenient results to explain the advance of rather different fronts such as several virus infections, the Neolithic transition and postglacial tree recolonizations. We have noted that our approximate speed $c = \sqrt{2D/T}$ is valid if high values of the reproduction rate are assumed. This suggests Eq. (5) could be a general trend in front propagation. Future work could report further applications of our simple approximate speed to other systems in which a lag time is important, e.g. crystallization fronts [32], combustion fronts (where the ignition time plays the role of the lag T) [33], etc.

Acknowledgments

Discussions with N. Isern and T. Pujol are acknowledged. This work was supported by the MICINN-FEDER (projects SimulPast-Consolider-CSD-2010-00034, FIS-2009-13050 and FIS-2012-31307) and by the Generalitat de Catalunya (Grup consolidat 2009-SGR-374).

Appendix A. Exact equations, numerical simulations and empirical data for virus infections

In the main text, Eqs. (1)–(4) are used to model the invasion front of several focal infection systems (then $[V]$ replaces p in Eq. (1)). In such experiments cells are not able to diffuse because they are immobilized by agar [9]. Hence, Eqs. (2) and (3) contain reactive but not diffusive terms. Viruses are the only species able to diffuse in the system; see Eq. (1). In order to compute the invasion speed, we introduce a frame moving with the front and look for solutions depending only on the new variable $z \equiv r - ct$, where $c > 0$ is the front speed. As usual, we linearize our Eqs. (1)–(4) around the unstable steady state $([V], [C], [I]) = (0, C_0, 0)$. Hence we consider $([V], [C], [I]) = (\epsilon_V, 1-\epsilon_C, \epsilon_I)C_0$ at the front edge, where $\overrightarrow{\epsilon} = (\epsilon_V, \epsilon_C, \epsilon_I) = \overrightarrow{\epsilon}_0 \exp(-\lambda z)$. For non-trivial solutions $(\epsilon_V, \epsilon_C, \epsilon_I) \neq (0, 0, 0)$ to exist, the determinant of the matrix corresponding to the linearized set of three evolution equations must vanish. Therefore, the following characteristic equation must be satisfied:

$$\lambda^3 + \frac{-\alpha^2 c^2\,(1-\beta)+1}{\alpha c(1-\alpha^2\beta c^2)}\lambda^2 + \frac{\kappa\,(\beta\kappa-1)+\beta\kappa Y-1}{1-\alpha^2\beta c^2}\lambda + \frac{(1-\beta\kappa)\,(\kappa Y-\kappa)}{\alpha c(1-\alpha^2\beta c^2)} = 0, \tag{20}$$

where $\alpha = (k_2 D)^{-1/2}$, $\beta = T/2$ and $\kappa \equiv k_1 C_0/k_2$.

[3] The values of Δ considered in this paper correspond to long-distance jumps, which produce a much more important effect on the front speed than short-distance jumps (see Ref. [22]).

[4] However, this was exactly the expected result, since high values of Y and T were assumed to derive Eq. (5) [11].

Table A.1
Parameter values applied to compute the invasion speeds of VSV and T7 infections in the main text, using both analytical solutions and numerical integrations of Eqs. (1)–(4).

	VSV	T7 (wild)	T7 (p005)	T7 (low-yield hypothesis)
D (cm^2/h)	1.44×10^{-4}	$8.55 \cdot 10^{-5}$	$8.55 \cdot 10^{-5}$	$8.55 \cdot 10^{-5}$
k_1 (cm^3/h)	1.4×10^{-10}	$7.74 \cdot 10^{-8}$	$7.74 \cdot 10^{-8}$	$7.74 \cdot 10^{-8}$
k_2 (h^{-1})	2.47	83.4	44.5	83.4
Y	4389	34.5	63.6	5

According to marginal stability analysis [23], the wave front speed can be finally calculated numerically from

$$c = \min_{\lambda>0}[c(\lambda)]. \tag{21}$$

This summarizes the computation of the exact infection front speed from Eqs. (1)–(4) (full symbols in Fig. 1). Usually dimensionless variables are used, but the final equations for the front speed are still rather complicated. Details, exact and approximate results can be found in our previous Ref. [11].

Besides the exact speed summarized above (full symbols in Fig. 1) and the approximate speed $c = \sqrt{2D/T}$ (curves in Fig. 1), simulated speeds have been obtained by integrating numerically the set of Eqs. (1)–(4) (empty symbols in Fig. 1). In order to do so, we have used finite differences to approximate the partial derivatives in Eqs. (1)–(4). Typical values for the space and time steps used in our simulations were below 1 μm and below 1 s, respectively. All simulations considered the initial conditions $[C] = C_0$ and $[I] = 0$ everywhere, and a viral concentration of $[V] = 9.3 \times 10^8$ /ml in a small central region with a radius of 0.075 cm [34] (this region represents the initial inoculum starting the focal infection).

In this paper we have studied infections of both VSV and T7 viruses (including mutants for the latter). VSV infections infect mammalian cells, whereas T7 viruses infect bacteria. We have used VSV and T7 infections because these are the only ones for which front speeds have been measured experimentally [8,9]. Table A.1 contains the parameter values used to compute the invasion speed.

For VSV, the parameter values in Table A.1 are the same as in Ref. [11] (to the best of our knowledge, no experimental data on the adsorption rate of the VSV are available, but the front speed is independent of the value of k_1 for several orders of magnitude [11]). For the wild type of T7, we use the values of k_1, k_2 and Y derived in Ref. [3] from experimental data. Using the same procedure as in Ref. [3], we have computed k_2 and Y for the T7 p005 mutant from the experimental data in Ref. [9] (the other parameter values are the same as for the wild T7 strain). The last column in Table A.1 corresponds to a low-yield hypothetical case of the T7 wild strain, which appears in Fig. 1 in the main text and is considered only to understand better the results there. The values of the diffusivity D in Table A.1 are based on the diffusivity of the P22 virus in agar, $D = 1.44 \cdot 10^{-4}$ cm^2/h [3]. Since the P22 virus is similar in size and shape to the VSV [11] and T7 viruses [3], it provides convenient approximations for the diffusivities of the viruses analyzed here. In Ref. [3] it was noticed that the presence of host cells in the medium actually hinders virus diffusion. To account for this effect, a convenient correction factor for the diffusivity of the virus must be computed (see Section V in Ref. [3]). In the present paper we consider the data from Ref. [9], so the bacterial concentration is $3 \cdot 10^6$ /ml, and the maximum possible bacterial concentration is 10^7 /ml. Thus, after taking into account the hindered-diffusion correction factor in Ref. [3] we obtain $D = 8.55 \cdot 10^{-5}$ cm^2/h for T7 viruses. In the case of VSV, experiments [8], there are no data indicating any hindered-diffusion effect; hence in Table A.1 we have considered free diffusion for VSV (as in Refs. [11,34]). According to the data from Ref. [9], the speed range for the T7 is 0.016–0.027 cm/h (from the minimum and maximum values in Figs. 4b and c in this reference). Note that the range of speed of the mutant p005 (Fig. 4b in Ref. [9]) widely overlaps with the range for the wild type (Fig. 4c in Ref. [9]). Thus, in our Fig. 1, we have used a single range for T7 viruses. In our previous paper [11] we estimated the experimental speed of VSV infections from the data in Fig. 2b in Ref. [8]. This led us to the experimental range of 0.066–0.08 cm/h [11]. However, additional data on infection profiles of the same experiments are available in Fig. S3 in Ref. [34], so in Table A.1 we take into account that a more realistic minimum experimental speed is 0.056 cm/h (from the evolution of the experimental radial profiles in Ref. [34]). The maximum value for the experimental speed is the same we proposed in Ref. [11], namely 0.08 cm/h.

Appendix B. Numerical simulations for the Neolithic transition

For the numerical simulations in Fig. 2, we have used a very simple model proposed in Ref. [14]. We consider a 2D square grid with the initial condition $p(x, y, t = 0) = p_{\max}$ at the central node, and $p(x, y, t = 0) = 0$ everywhere else in the square grid. Each time step in the simulations represents an interval time of $T = 1$ generation. At every time step, the population density is equally distributed into the 8 nearest neighbors, so the mean-squared displacement is

$$\langle \Delta^2 \rangle = \frac{1}{8} \sum_{j=0}^{1} 4\left[d^2 + (jd)^2\right], \tag{22}$$

where d is the distance between two neighboring nodes. Also, we compute the effect of population growth at each node and each time step by applying the solution for the logistic growth given by Eq. (11),

$$R_T[p(x, y, t)] = \frac{p(x, y, t) p_{\max} e^{aT}}{p_{\max} + p(x, y, t)\left(e^{aT} - 1\right)}. \tag{23}$$

Finally, the population density at each node for the next step $p(x, y, t+1)$ is computed as the sum of $R_T[p(x, y, t)]$ and the dispersive contribution described above.

Appendix C. Matrix elements, empirical data and numerical simulations for postglacial tree recolonizations

The following considerations have been applied to the matrices in the structured population model for tree recolonizations in Section 3. The demographic matrix $\overrightarrow{\overrightarrow{A}}$ describes reproduction and aging of the population as follows. The elements of $\overrightarrow{\overrightarrow{A}}$ take into account that (i) each adult tree produces yearly a surviving number of seeds R_0 and (ii) individuals become one year older by switching its stage from j to $j+1$ at each time increment $t \dashrightarrow t+1$. Thus, $\overrightarrow{\overrightarrow{A}}$ is written as [19]

$$A_{ij} = \begin{cases} R_0 & \text{if } i = 1,\ j \geq T \\ 1 & \text{if } i = j+1 \\ 0 & \text{otherwise,} \end{cases} \tag{24}$$

where R_0 is the mean fecundity (i.e., number of seeds that survive into an adult tree) per parent tree and year.

The elements Φ_{ij} of the dispersal matrix $\overrightarrow{\overrightarrow{\Phi}}$ describe the rate of every possible conversion of $p_i(x+\triangle_x, y+\triangle_y, t)$ into $p_j(x, y, t+1)$. Since $\overrightarrow{\overrightarrow{\Phi}}$ must restrict dispersal to new individuals (trees do not move but only disperse seeds), the elements of $\overrightarrow{\overrightarrow{\Phi}}$ are [19]

$$\Phi_{ij} = \begin{cases} \phi(\Delta_x, \Delta_y) & \text{if } i = 1,\ j \geq T \\ \delta_{2D}(\Delta) & \text{otherwise,} \end{cases} \tag{25}$$

where $\delta_{2D}(\Delta)$ is the two-dimensional Dirac delta centered at $\Delta = 0$. The dispersal kernel $\phi(\triangle_x, \triangle_y)$ is the probability per unit area that a seed falling from a parent tree located at $(x+\triangle_x, y+\triangle_y)$ reaches the ground at (x, y) [19].

For the computations in Fig. 3a and b in the present paper, we have considered the same isotropic kernel as in Ref. [19], i.e. that new seeds of the yellow poplar either grow in the same location as the parent tree (with probability $p_e = 0.99798$ [22]) or they are dispersed to a distance $r = \Delta$ (with probability $1 - p_e$). Moreover, the annual seed production f of the yellow poplar is of the order of 10^4 seeds dispersed/tree yr [30,25]. According to field observations in sites close to those where the dispersal kernel was measured, the yellow poplar postdispersal seed-to-adult survival is in the range 0.00–0.06% [30,35]. In the present work we have considered the mean value of this survival rate, i.e., $s = 0.03\%$. Thus, we estimate the net reproductive rate, $R_0 = fs$, to be in the range of 3–30 seeds/tree yr for the yellow poplar.

To the best of our knowledge, there is no available data on the long-distance dispersal kernel of the black alder. However, long-distance dispersals are usually driven by extreme climatological conditions (and they are independent of the usual dispersal agency of the seed) [31]. Thus, we expect the persistence p_e of the black alder to be of the same order of magnitude than the one for the yellow poplar. We have used $p_e = 0.99798$ [22] in the isochrone map for the black alder in Fig. 3c. The observed annual seed production f of this species is of the order of 10^4 seeds dispersed/tree yr [26]. For the case of the black alder, we consider the survival probability $s = 0.03\%$ (i.e., the same considered for the seeds of the yellow poplar), since we are not aware of any specific observed range for the black alder. This yields an estimated net reproductive rate, $R_0 = fs$, in the range of 3–30 seeds/tree yr for the black alder. Since our approximate speed $c = \sqrt{2D/T}$ assumes high values of the reproduction rate (see the discussion above), in Fig. 3c we have considered the highest value in this range, i.e., $R_0 = 30$ seeds/tree yr.

Results from molecular dynamics simulations have been presented as empty symbols in Fig. 3a, b. Our computer program considers a 2D grid where an age-structured population density is computed. Initially $p(x, y, 0) = 1$ at $(x, y) = (0, 0)$ and $p(x, y, 0) = 0$ elsewhere. At each time step, we compute the new number density of trees $p(x, y, t+1)$ at all nodes. The main features of this model (immature individuals cannot reproduce, etc.) are properly taken into account (we refer the interested reader to Ref. [19] for further details about these molecular dynamics simulations).

References

[1] J. Merikoski, J. Maunuksela, M. Myllys, J. Timonen, M.J. Alava, Temporal and spatial persistence of combustion fronts in paper, Phys. Rev. Lett. 90 (2) (2003) 024501.
[2] S.J. Di Bartolo, A.T. Dorsey, Velocity selection for propagating fronts in superconductors, Phys. Rev. Lett. 77 (21) (1996) 4442–4445.
[3] J. Fort, V. Méndez, Time-delayed spread of viruses in growing plaques, Phys. Rev. Lett. 89 (17) (2002) 178101.
[4] S. Fedotov, A. Iomin, Migration and proliferation dichotomy in tumor cell invasion, Phys. Rev. Lett. 98 (11) (2007) 118101.
[5] J. Fort, V. Méndez, Time-delayed theory of the Neolithic transition in Europe, Phys. Rev. Lett. 82 (4) (1999) 867–870.
[6] N. Isern, J. Fort, Time-delayed reaction–diffusion fronts, Phys. Rev. E 80 (5) (2009) 057103.
[7] R.A. Fisher, The wave of advance of advantageous genes, Ann. Eugen. 7 (1937) 355–369.
[8] V. Lam, K.A. Duca, J. Yin, Arrested spread of vesicular stomatitis virus infections in vitro depends on interferon-mediated antiviral activity, Biotech. Bioeng. 90 (7) (2005) 793–804.
[9] J. Yin, Evolution of bacteriophage T7 in a growing plaque, J. Bacteriol. 175 (5) (1993) 1272–1277.
[10] V. Ortega-Cejas, J. Fort, V. Méndez, D. Campos, Approximate solution to the speed of spreading viruses, Phys. Rev. E 69 (3) (2004) 031909.

[11] D.R. Amor, J. Fort, Virus infection speeds: theory versus experiment, Phys. Rev. E 82 (6) (2010) 061905.
[12] R. Pinhasi, J. Fort, A.J. Ammerman, Tracing the origin and spread of agriculture in Europe, PLOS Biol. 3 (12) (2005) e410.
[13] J.D. Murray, Mathematical Biology, vol. 1, third ed., Springer-Verlag, Berlin, 2002, pp. 1–6.
[14] N. Isern, J. Fort, J. Pérez-Losada, Realistic dispersion kernels applied to cohabitation reaction–dispersion equations, J. Stat. Mech. Theory Exp. (10) (2008) P10012.
[15] J. Fort, D. Jana, J. Humet, Multidelayed random walks: theory and application to the neolithic transition in Europe, Phys. Rev. E 70 (3) (2004) 031913.
[16] J.B. Birdsell, Some population problems involving Pleistocene man, Cold Spring Harb. Symp. Quant. Biol. 22 (1957) 47–69.
[17] D.F. Roberts, Genetic effects of population size reduction, Nature 220 (5172) (1968) 1084–1088.
[18] A.J. Lotka, Elements of Mathematical Biology, Dover, New York, 1956, pp. 64–69.
[19] D.R. Amor, J. Fort, Fronts from two-dimensional dispersal kernels: beyond the nonoverlapping-generations model, Phys. Rev. E 80 (5) (2009) 051918.
[20] M. Neubert, H. Caswell, Demography and dispersal: calculation and sensitivity analysis of invasion speed for structured populations, Ecology 81 (6) (2000) 1613–1628.
[21] Y.M. Buckley, E. Brockerhoff, L. Langer, N. Ledgard, H. North, M. Rees, Slowing down a pine invasion despite uncertainty in demography and dispersal, J. Appl. Ecol. 42 (2005) 1020–1030.
[22] J. Fort, Fronts from complex 2D dispersal kernels. Theory & application to Reid's paradox, J. Appl. Phys. 101 (9) (2007) 094701.
[23] U. Ebert, W. van Saarloos, Front propagation into unstable states: universal algebraic convergence towards uniformly translating pulled fronts, Physica D 146 (2000) 1–99.
[24] J.S. Clark, M. Lewis, L. Horvath, Invasion by extremes: population spread with variation in dispersal and reproduction, Am. Nat. 157 (5) (2001) 537–554.
[25] D.E. Beck, Liriodendron tulipifera, in: R.M. Burns, B.H. Honkala (Eds.), Silvics of North America, in: Agriculture Handbook 654, vol. 2, USDA Forest Service, Washington, DC, 1990, pp. 406–416.
[26] A. Harrington, L.S. Brodie, D.S. DeBell, C.S. Schopmeyer, Alder, in: F.T. Bonner, R.P. Karrfalt (Eds.), The Woody Plant Seed Manual, in: Agriculture Handbook, vol. 727, USDA Forest Service, Washington, DC, 2008, pp. 232–242.
[27] Seeds of Alnus glutinosa are typically water-dispersed [28]. However, long-distance dispersals are rare events which produce long migrations independently of the usual dispersal agency of the seed [31]. Therefore, as in the case for Liriodendron tulipifera (Fig. 3a, b), migrations in the range 10^3–10^4 m are expected for the Alnus glutinosa.
[28] H.J.B. Birks, Holocene isochrone maps and patterns of tree-spreading in the British Isles, J. Biogeography 16 (1989) 503–540.
[29] J.S. Clark, Why trees migrate so fast: confronting theory with dispersal biology and the paleorecord, Am. Nat. 152 (2) (1998) 204–220.
[30] R. Nathan, G.G. Katul, H.S. Horn, S.M. Thomas, R. Oren, R. Avissar, S.W. Pacala, S.A. Levin, Mechanisms of long-distance dispersal of seeds by wind, Nature 418 (6896) (2002) 409–413.
[31] R. Nathan, F.M. Schurr, O. Spiegel, O. Steinitz, A. Trakhtenbrot, A. Tsoar, Mechanisms of long-distance seed dispersal, Trends Ecol. Evol. 23 (11) (2008) 638–641.
[32] P.K. Galenko, D. Danilov, Selection of the dynamically stable regime of rapid solidification front motion in an isothermal binary alloy, J. Cryst. Growth 216 (4) (2000) 512–536.
[33] T. Kashiwagi, K.B. McGrattan, S.L. Olson, O. Fujita, M. Kikuchi, K. Ito, Effects of slow wind on localized radiative ignition and transition to flame spread in microgravity, in: Combustion Institute, 26th Proceedings of the Symposium (International) on Combustion, (Napoli, Italy), vol. 1, Combustion Institute, Pittsburgh, 1996, pp. 1345–1352.
[34] L. Haseltine, V. Lam, J. Yin, J.B. Rawlings, Image-guided modeling of virus growth and spread, Bull. Math. Biol. 70 (2008) 1730–1748.
[35] D. De Steven, Experiments on mechanisms of tree establishment in old-field succession: seedling survival and growth, Ecology 72 (3) (1991) 1076–1088.